scientific reports

OPEN

Magnetic NiFe thin films composing MoS$_2$ nanostructures for spintronic application

Mahdi Yousef Vand[1,2], Loghman Jamilpanah[2], Mohammad Zare[2] & Seyed Majid Mohseni[2✉]

We demonstrate a nanostructure layer made of Ni$_{80}$Fe$_{20}$ (permalloy:Py) thin film conjugated MoS$_2$ nano-flakes. Layers are made based on a single-step co-deposition of Py and MoS$_2$ from a single solution where ionic Ni and Fe and MoS$_2$ flakes co-exist. Synthesized thin films with MoS$_2$ flakes show increasing coercivity and enhancement in magneto-optical Kerr effect. Ferromagnetic resonance linewidth as well as the damping parameter increaseed significantly compared to that of the Py layer due to the presence of MoS$_2$. Raman spectroscopy and elemental mapping is used to show the quality of MoS$_2$ within the Py thin film. Our synthesis method promises new opportunities for electrochemical production of functional spintronic-based devices.

Recent promising achievements in spintronics specially in magnetic thin films conjugated to two-dimensional (2D) materials has made this topic interesting for fundamental studies to explore their important role in the future spintronic-based memory and computing devices[1–5]. The core deriving fundamental phenomenon in such structures is the spin–orbit interaction (SOI)[6,7]. To benefit from SOI in spintronic devices, materials with high spin–orbit coupling (SOC), mostly heavy metals like Pt and Ta[8] are used in devices in contact to magnetic thin films. Also, due to the recent developments in the field of 2D materials, special focus is put into implementing 2D materials with their intriguing properties instead of those heavy metals[9,10] with high SOC. Many studies have demonstrated the successful usage of transition metal dichalcogenides (TMDCs) in contact to ferromagnetic thin films to enhance the SOI, induce surface anisotropy, etc.[11,12]. We have recently demonstrated that the magnetic anisotropy can be tuned by MoS$_2$ on the surface of Py thin films[13] and also predicted interfacial anisotropy can be changed in Co/black-phosphorene[14]. Here, we alternatively demonstrate the magnetic properties of Ni$_{80}$Fe$_{20}$ change by embodiment of MoS$_2$ thin flakes. This shows the whole single ferromagnetic thin film to possess SOC-induced intrinsic magnetic properties.

Fabrication of thin films for spintronics devices based on physical techniques such as sputtering and thermal evaporation have shown the best performance[15,16]. Besides, electrodeposition method has established to be very promising in producing spin valves with very high number of layer repetitions (above 100 repeated layers[17]) and also functional nanowires for spin caloritronic devices[18–20]. Although it should be mentioned that electro-deposition lacks the ability to provide ultra-thin films without voids or making multilayers of diverse types of materials in a single growth[21]. The implementation of 2D materials in contact to ferromagnetic thin films has been challenging[22,23] and such structures are made by transferring the as-made 2D layers on the ferromagnetic layers[24]. In addition to their multi-step fabrication method, the materials contacts are poor that hitherto limits their reproducibility and scalability[25]. Therefore, developing new fabrication method for making heterostructure of 2D materials/ferromagnetic layers is demanded to achieve higher yield and functionality.

In this work, we use electrodeposition method for fabrication of Py magnetic films and present the co-electro-deposition of MoS$_2$ thin flakes with ionic elements of the solution. The Raman spectroscopy indicates successful embodiment of thin MoS$_2$ flakes inside the grown magnetic film. The magnetic properties of the layer with MoS$_2$ flakes show prominent differences with bare ferromagnetic layer including higher magnetic coercivity and damping parameter which are directly related to the enhancement in SOC of the medium. Our results indicate that our fabrication method has resulted in a good proximity between the MoS$_2$ and the magnetic material for inducing SOC in the ferromagnet. Our method has the possibility of being used for growth of gradients or multilayers of the investigated material through control of the growth conditions like applied growth voltage/current.

[1]Materials Engineering, Faculty of Engineering, University of Tehran, Tehran, Iran. [2]Department of Physics, Shahid Beheshti University, Evin, Tehran 19839, Iran. ✉email: m-mohseni@sbu.ac.ir
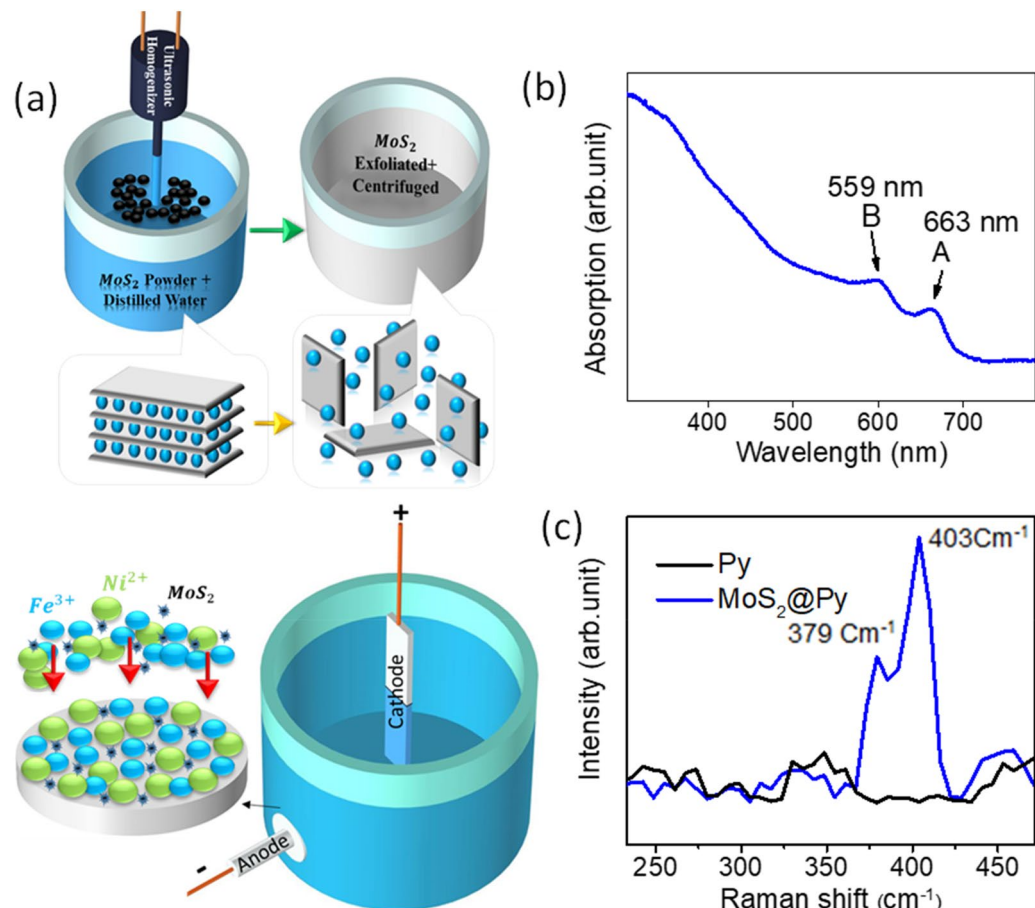
Figure 1. (**a**) Schematic of the MoS_2 exfoliation by probe sonication (above) and the schematic of electrodeposition of samples (below). (**b**) The UV–Visible absorption of the exfoliated MoS_2 and (**c**) the Raman spectrum of Py and MoS_2@Py samples.

Experimental section

Exfoliation of MoS_2. Exfoliation of MoS_2 was done for a 1 g MoS_2 powder (Aldrich, 99%, < 2 μm) in 100 ml distilled water, equivalent to 10 g l^{-1} concentrations of MoS_2 (Fig. 1a). The MoS_2 powder was exfoliated for 4 h using a sonication probe unit equipped with a long step horn tip. In order to avoid excessive heating, the probe of sonic was set to operate 0.7 s and rest for 0.3 s and also an ice-water bath was used during the exfoliation. The resulting solution was centrifuged for 30 min at 200 rpm to remove non-exfoliated particles.

Electrodeposition. Electrodeposition was done from two different solutions. First solution for electrodeposition of the Py sample had the composition of 0.4 M $NiSO_4.6H_2O$, 0.04 M $FeSO_4.7H_2O$, and 0.4 M H_3BO_3 (originally prepared from Merk) in distilled water. 200 ml of this solution was used for the electrodeposition. For the electrodeposition of the Py conjugated MoS_2 sample (MoS_2@Py), second solution was prepared as the following. First a 100 ml of the same solution with doubled molarities was prepared and then a 100 ml of the exfoliated MoS_2 solution was added to it. This way the final molarities of Ni and Fe ions is similar in both the solutions. Si substrates (single side polished surface) were cut by 1.5 × 1.5 cm slices. In order to clean surface of the Si from native oxide, they were dipped in 10% HF (hydrochloric acid) solution for 45 s, then washed by ethanol, acetone and distilled water respectively, and dried by air pump. Then the Si substrates were immediately transferred to the electrodeposition cell to prevent further surface oxidation. A two-electrode cell configuration with a DC current source was used for the electrodepositions. A 2 × 1 cm platinized Si was used as the anode and Si substrate as the cathode. The Py and MoS_2@Py samples were electrodeposited by applying a direct voltage of 10 V at room temperature during 120 and 150 s, respectively.

Characterization. UV–Visible (Perkin Elmer, Lambda25) and Raman spectroscopy (Teksan) were carried out at room temperature. Surface was probed via atomic force microscopy (AFM, nanosurf) measurement. Energy dispersive X-ray spectroscopy (EDX) and elemental mapping were measured by through field emission scanning electron microscope (FESEM, Hitachi). Magnetic hysteresis loops were measured by longitudinal magneto-optical Kerr effect (MOKE), with a 632 nm laser light (a home-made setup). Ferromagnetic resonance

(FMR) measurements were performed by a home-made field modulation lock-in technique at the frequency range of 2–20 GHz (for details see supporting information).

Results

Schematic of the exfoliation condition is depicted in Fig. 1a where the force of water molecules results in exfoliation of the MoS_2 powder into thin flakes. To characterize the quality of the exfoliated MoS_2 in water, UV–Visible absorption measurement was used. Result of this measurements can be seen in Fig. 1b. The A and B peaks at 559 and 663 nm respectively are the characteristic of few layer MoS_2 dispersions. After solution preparation and electrodeposition of the layers (Fig. 1a below) Raman characterization is used to see if the MoS_2 flakes are imbedded in the body of the Py layer. Figure 1c presents the Raman spectrum for Py and MoS_2@Py samples. Raman peaks at 379 and 403 cm^{-1} clearly show the presence of MoS_2 flakes in the electrodeposited layer[26]. The bare Py sample shows no peak in its Raman spectrum because it has a metallic nature.

The surface topography of the Py and MoS_2@Py samples has been observed with AFM and presented in Fig. 2a and b, respectively. The AFM images show that both samples have a similar surface structure with an increased mean surface roughness for the MoS_2@Py sample to 45 nm from the 20 nm mean surface roughness of the Py sample. Also, FESEM characterization of the Py and MoS_2@Py samples has been performed and results are presented in Fig. 2c and d, respectively. It can be seen that both the samples have a granular structure with an increased grain size for the MoS_2@Py sample. Also cross sectional FESEM images of the samples are presented in supporting information which show thicknesses of ~ 50 and ~ 100 nm for Py and MoS_2@Py samples (~ 10% error), respectively. The observed higher thickness of the MoS_2@Py samples is related to the partial space occupation by MoS_2 and also the slightly higher electrodeposition time of this sample. Distribution of MoS_2 in Py layer has been evidenced by EDX measurement. Figure 2e–h represents the EDX mapping of Ni, Fe, Mo and S elements where the uniform color distribution shows the uniform embodiment of MoS_2. Also, the atomic ratio of Ni:Fe is 4:1.

In continue, magnetic properties of the samples are investigated through the MOKE and FMR measurements. Longitudinal MOKE measurement results are presented in Fig. 3a showing that both the samples have an in-plane magnetic anisotropy. Two prominent differences are appeared in the MOKE signal of the samples. One is the much higher coercivity (H_c) of the MoS_2@Py sample which is depicted in Fig. 3b. The H_c for the Py sample is ~ 10 Oe and has increased to ~ 30 Oe for the MoS_2@Py sample which is equivalent to a 300% increase. In the case of films, the magnetic anisotropy of ferromagnetic layers has been demonstrated to change by proximity to TMDC layered materials due to the d-d hybridization at the interface[11,13,14]. In the case of MoS_2@Py sample, all interfacial directions between Py and MoS_2 is possible which overall has resulted in the observed in-plane coercivity change. Generally, magnetic anisotropy is highly dependent on the SOC[27–29] and by addition of MoS_2 as a material with high SOC to the layer, changes in the magnetic anisotropy is expected. One should note that increase of the in-plane coercivity can result from the increase of thickness because of the emerging out of plane magnetic anisotropy component at higher thicknesses[30–34]. To see if the observed increase of H_c in our samples is due to the relatively higher thickness of the MoS_2@Py sample we performed MOKE measurements for different thicknesses of Py layer and only a slight change in the H_c was observed (for the details see supporting information). Therefore, we conclude that the observed changes in the magnetic properties of Py is due to its proximity to MoS_2. Also, the H_c of the samples can be affected by the grain size[35] and the AFM and SEM images indicate a comparably bigger grain size for the MoS_2@Py sample. But the totally different MOKE signal quality of the MoS_2@Py sample, including the slope of the plot, indicates that presence of MoS_2 is playing a crucial role in this increased H_c.

The other observation from the MOKE signal is the much higher signal intensity of the MoS_2@Py sample relative to Py sample which is increased by 275%. Two mechanism can play role in the observed MOKE signal increase for the MoS_2@Py sample: (1) increase of the saturation magnetization (M_s) and (2) increase of light interaction with matter[36,37]. Here the increase of the MOKE signal cannot be due to the increase of M_S, as the M_S decreases for the MoS_2@Py sample (See FMR section). Therefore, increase of the MOKE signal can be related to the increased interaction between light and the MoS_2@Py sample. For the case of multilayered ferromagnet/TMDC heterostructures it has been reported that proper thickness, refraction index and incident angle, can form a cavity[38,39]. Here we achieved enhancement of the MOKE signal via composing MoS_2 flakes with the magnetic layer. Enhancement of light-mater interaction also has been achieved via electrophoretic deposition of MoS_2 nanostructures[40]. Simulation of the MOKE signal for the composed MoS_2@Py sample are encouraged to obtain the optimized composing structure. Also, we do not ignore the possibility of the larger grain size in the MoS_2@Py being responsible partially for the observed MOKE signal intensity increase. For determining the exact contribution of each parameter further experiments should be designed.

We have also measured the FMR characteristics of the samples to see how MoS_2 can affect the magnetization dynamics of the Py layer. The spin dynamic response of the samples investigated at different constant microwave frequencies ranging from 2 to 20 GHz and by sweeping H from 0 to 4500 Oe. The observed FMR spectra were fitted with the derivative of Lorentzian function to determine the resonance field (H_r) and FWHM (ΔH) at each frequency. Figure 3c presents the measured FMR signal of the samples (dots) and their fit (solid line) at $f = 14$ GHz. The frequency dependence of H_r for the Py and MoS_2@Py samples can be seen in Fig. 3d (dots). The solid lines in this figure are the fitted data by Kittel's equation. Dependence of the FMR frequency on the external magnetic field for thin films assuming with infinite dimensions which are saturated in the plane can be described by Kittel formula[41],

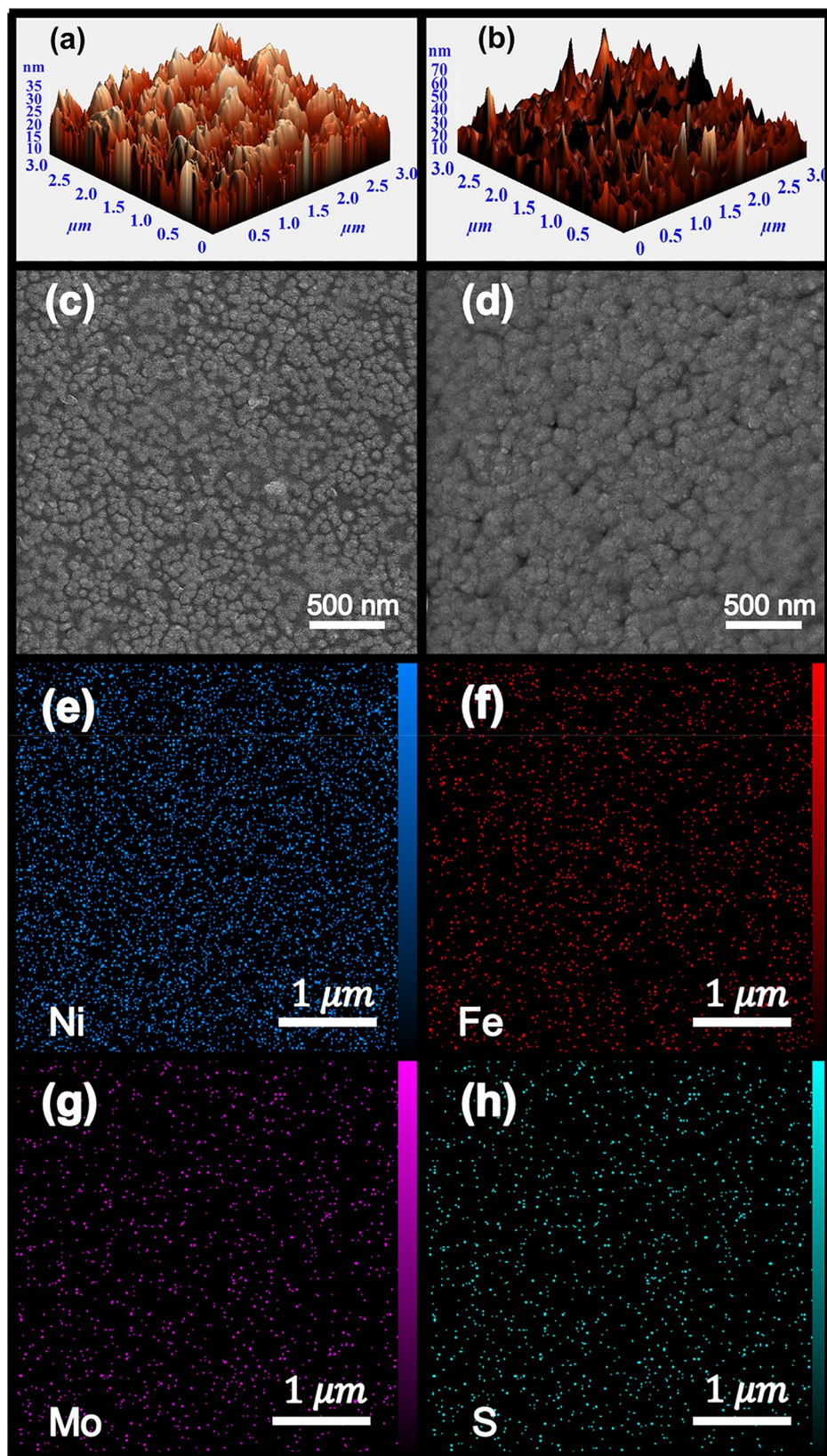$$f_r = \frac{\mu_0 \gamma}{2\pi} \sqrt{(H + H_k + M_s)(H + H_k)}$$

Figure 2. AFM measurement of (**a**) Py and (**b**) MoS$_2$@Py samples. The FESEM images of (**c**) Py and (**d**) MoS$_2$@Py samples. (**e**) and (**f**) are the EDX mapping of Py sample and (**g**) and (**h**) the EDX mapping of the MoS$_2$@Py sample.
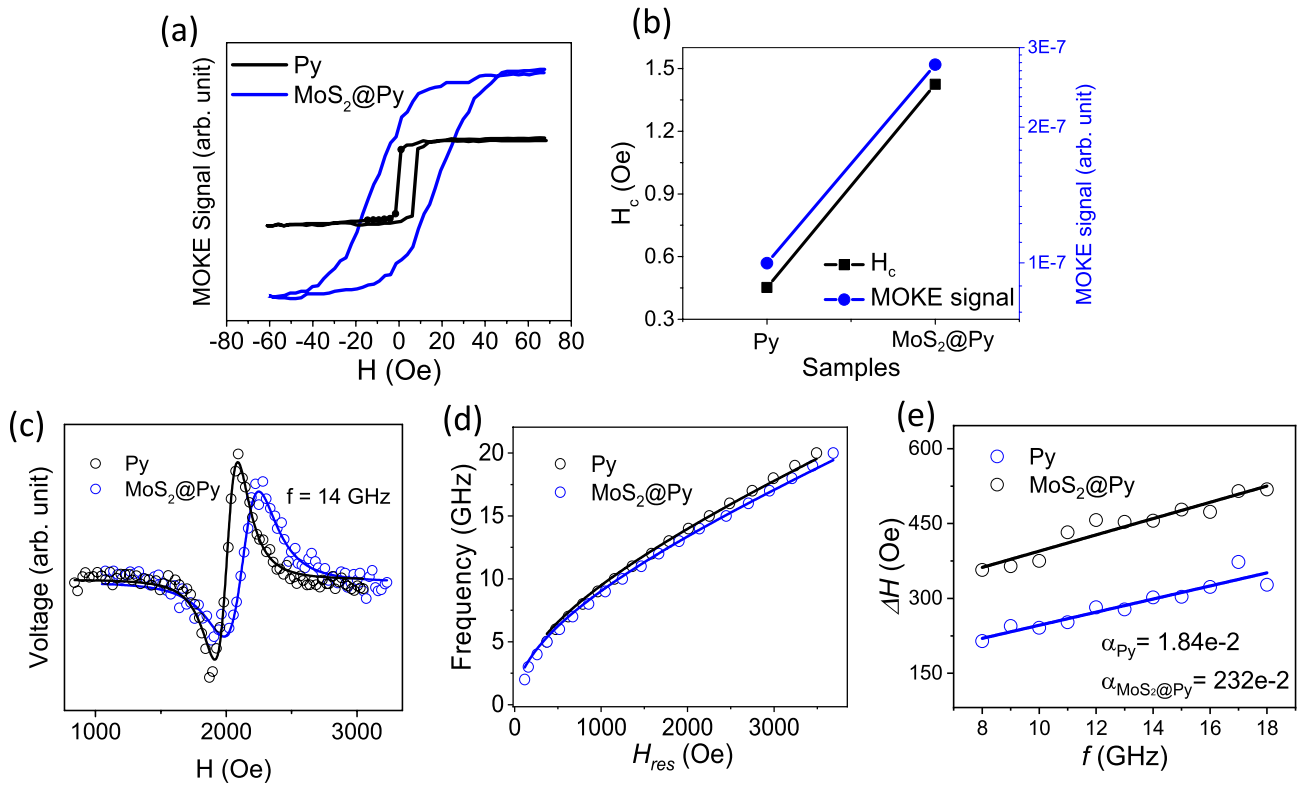
www.nature.com/scientificreports/

Figure 3. (**a**) MOKE signal measured for the samples and (**b**) comparison of the H_c and the MOKE signal intensity of the samples. (**c**) the FMR signal observed at f = 14 GHz, (**b**) the fitted f and H_{res} curve based on Kittel formula and (**c**) the data of FWHM versus f and their fitting based on the damping relation.

	Py	MoS$_2$@Py
α	0.018	0.023
M_s (Oe)	10,448	9391
γ	0.0028	0.0028
H_k (Oe)	0	0
ΔH_0 (Oe)	114	231

Table 1. The α, M_s, γ, H_k, ΔH_0 obtained from the fitting of FMR data.

where μ_0 is the permeability of the free space, γ is the gyromagnetic ratio (28 GHz/Tesla), H is the external magnetic field and H_k is the uniaxial anisotropy field which is negligible for Py films with low thickness. The resulted M_S from this fit are 10,448 and 9391 Oe for the Py and MoS$_2$@Py samples, respectively. A decrease of about 10% in the M_s of the MoS$_2$@Py sample is observed which can be understood via the nonmagnetic character of the MoS$_2$ that results in a lower magnetization per unit volume. Also, both samples do not show magnetic anisotropy. By using the damping relation[42], as the following:

$$\Delta H = \Delta H_0 + \frac{4\pi \alpha f}{\gamma}$$

and fitting the data we can calculate the damping parameter of the samples. Here ΔH_0 is the inhomogeneous broadening, and α is the Gilbert damping parameter. The fitting of the data based on this equation can be seen in Fig. 3e. The value of ΔH_0 for Py and MoS2@Py samples are 114 and 231 Oe respectively. All the obtained parameters from the FMR data are presented in Table 1.

In the obtained results, we see a doubling of the damping coefficient in the MoS$_2$@Py sample compared to the Py sample, which has increased from 0.018 to 0.023. There are many reports that show the coating of a nonmagnetic layer on a ferromagnetic layer can lead to the enhancement of the damping parameter[43-45]. Several mechanisms have been proposed for the enhancement of damping parameter in such bilayers. SOC and interfacial d-d hybridization cause the enhancement of the intrinsic damping, while extrinsic enhancement of the damping can arise from two-magnon scattering processes, due to roughness and defects at the interface region[46-48]. In the case of our sample, embodiment of MoS$_2$ in the Py layer results in the increased interfaces

between Py and MoS_2 and therefore both intrinsic and extrinsic contribution can contribute in the observed increase of the damping parameter. Moreover, the coupling between a FM layer and an adjacent NM layer can enhance the effective damping of the magnetization precession via spin-pumping effect[44,49]. For example, many groups have recently demonstrated the generation of spin–orbit torque in devices made with the Py/WTe$_2$[50], CoFeB/MoS$_2$ or WSe$_2$[51], and Py/MoS$_2$[52] and the reciprocal process (voltage generation from spin-pumping) in MoS_2/Al/Co heterostructures[53]. In the case of our MoS_2@Py sample we observe the phenomena via enhanced damping parameter in a relatively thick magnetic layer thanks to the embodiment of the MoS_2 flakes inside the layer which gives a high contact surface area between MoS_2 and Py.

Conclusions

MoS_2 was successfully embodied within the structure of the Py magnetic thin film by electrodeposition method. The layer with MoS_2 flakes shows a higher magnetic coercivity and Gilbert damping parameter, indicating the proper bonding between the MoS_2 and the magnetic material. In addition, the cavity of light in the MoS_2@Py sample resulted in a three-fold increase of the MOKE signal which opens a pathway for the research on the optimization of MOKE sensors and also fundamental studies in the field. Due to the capability of applying our method for a large set of ferromagnetic/TMDC materials, there is a great potential for further development of functional spintronic and magnonic devices.

References

1. Vega, V., Ferna, A., Prida, V. M., Salaheldeen, M. & Me, M. Tuning nanohole sizes in Ni hexagonal antidot arrays : Large perpendicular magnetic anisotropy for spintronic applications. *ACS Appl. Nano Mater.* https://doi.org/10.1021/acsanm.8b02205 (2019).
2. Ahn, E. C. 2D materials for spintronic devices. *NPJ 2D Mater. Appl.* **4**, 1–14 (2020).
3. Lin, X., Yang, W., Wang, K. L. & Zhao, W. Two-dimensional spintronics for low-power electronics. *Nat. Electron.* **2**, 274–283 (2019).
4. Avsar, A. *et al.* Colloquium: Spintronics in graphene and other two-dimensional materials. *Rev. Mod. Phys.* **92**, 021003 (2020).
5. Salaheldeen, M., Martínez-Goyeneche, L., Álvarez-Alonso, P. & Fernández, A. Enhancement the perpendicular magnetic anisotropy of nanopatterned hard/soft bilayer magnetic antidot arrays for spintronic application. *Nanotechnology* **31**, 485708 (2020).
6. Premasiri, K. & Gao, X. P. A. Tuning spin–orbit coupling in 2D materials for spintronics: A topical review. *J. Phys. Condens. Matter* **31**, 193001 (2019).
7. Shi, S. *et al.* All-electric magnetization switching and Dzyaloshinskii–Moriya interaction in WTe$_2$/ferromagnet heterostructures. *Nat. Nanotechnol.* **14**, 945–949 (2019).
8. Manchon, A. *et al.* Current-induced spin–orbit torques in ferromagnetic and antiferromagnetic systems. *Rev. Mod. Phys.* **91**, 035004 (2019).
9. Husain, S. *et al.* Emergence of spin–orbit torques in 2D transition metal dichalcogenides: A status update. *Appl. Phys. Rev.* **7**, 41312 (2020).
10. Ramaswamy, R., Lee, J. M., Cai, K. & Yang, H. Recent advances in spin–orbit torques: Moving towards device applications. *Appl. Phys. Rev.* **5**, 031107 (2018).
11. Zhang, W. *et al.* Ferromagnet/two-dimensional semiconducting transition-metal dichalcogenide interface with perpendicular magnetic anisotropy. *ACS Nano* **13**, 2253–2261 (2019).
12. Polesya, S., Mankovsky, S., Ködderitzsch, D., Bensch, W. & Ebert, H. Dzyaloshinskii–Moriya interactions and magnetic texture in Fe films deposited on transition-metal dichalcogenides. *Phys. Status Solidi Rapid Res. Lett.* **10**, 218–221 (2016).
13. Jamilpanah, L., Hajiali, M. & Mohseni, S. M. Interfacial magnetic anisotropy in Py/MoS$_2$ bilayer. *J. Magn. Magn. Mater.* **514**, 167206 (2020).
14. Hoseyni, S. H., Rahimi, K., Barakati, B., Sadeghi, A. & Mohseni, S. M. Magnetic anisotropy in Co/phosphorene heterostructure. *Phys. E Low-Dimens. Syst. Nanostruct.* **128**, 114620 (2021).
15. Salaheldeen, M. *et al.* Tailoring of perpendicular magnetic anisotropy in Dy$_{13}$Fe$_{87}$ thin films with hexagonal antidot lattice nanostructure. *Nanomaterials* https://doi.org/10.3390/nano8040227 (2018).
16. Hierro-Rodriguez, A. *et al.* Revealing 3D magnetization of thin films with soft X-ray tomography: Magnetic singularities and topological charges. *Nat. Commun.* **11**, 6382 (2020).
17. Bakonyi, I. & Péter, L. Electrodeposited multilayer films with giant magnetoresistance (GMR): Progress and problems. *Prog. Mater. Sci.* **55**, 107–245 (2010).
18. da Santa Clara Gomes, T. C., Abreu Araujo, F. & Piraux, L. Making flexible spin caloritronic devices with interconnected nanowire networks. *Sci. Adv.* **5**, eaav2782 (2019).
19. Abreu Araujo, F., da Câmara Santa Clara Gomes, T. & Piraux, L. Magnetic control of flexible thermoelectric devices based on macroscopic 3D interconnected nanowire networks. *Adv. Electron. Mater.* **5**, 1800819 (2019).
20. Piraux, L., da Câmara Santa Clara Gomes, T., Araujo, F. A. & de la Torre Medina, J. 3D magnetic nanowire networks. In *Magnetic Nano- and Microwires* (ed. Vázquez, M.) 801–831 (Elsevier, 2020). https://doi.org/10.1016/b978-0-08-102832-2.00027-x.
21. Torabinejad, V., Aliofkhazraei, M., Assareh, S., Allahyarzadeh, M. H. & Rouhaghdam, A. S. Electrodeposition of Ni–Fe alloys, composites, and nano coatings—A review. *J. Alloys Compd.* **691**, 841–859 (2017).
22. Megra, Y. T. & Suk, J. W. Adhesion properties of 2D materials. *J. Phys. D. Appl. Phys.* **52**, 364002 (2019).
23. Torres, J., Zhu, Y., Liu, P., Lim, S. C. & Yun, M. Adhesion energies of 2D graphene and MoS$_2$ to silicon and metal substrates. *Phys. Status Solidi Appl. Mater. Sci.* **215**, 1700512 (2018).
24. Sklenar, J. *et al.* Perspective: Interface generation of spin–orbit torques. *J. Appl. Phys.* **120**, 7514–7520 (2016).
25. Lv, W. *et al.* Electric-field control of spin–orbit torques in WS$_2$/permalloy bilayers. *ACS Appl. Mater. Interfaces* **10**, 2843–2849 (2018).
26. Windom, B. C., Sawyer, W. G. & Hahn, D. W. A Raman spectroscopic study of MoS$_2$ and MoO$_3$: Applications to tribological systems. *Tribol. Lett.* **42**, 301–310 (2011).
27. Scherer, D. D. & Andersen, B. M. Spin–orbit coupling and magnetic anisotropy in iron-based superconductors. *Phys. Rev. Lett.* **121**, 037205 (2018).
28. Jansen, H. J. F. Magnetic anisotropy in density-functional theory. *Phys. Rev. B Condens. Matter Mater. Phys.* **59**, 4699–4707 (1999).
29. Shick, A. B., Khmelevskyi, S., Mryasov, O. N., Wunderlich, J. & Jungwirth, T. Spin–orbit coupling induced anisotropy effects in bimetallic antiferromagnets: A route towards antiferromagnetic spintronics. *Phys. Rev. B Condens. Matter Mater. Phys.* **81**, 212409 (2010).

30. Miao, G., Xiao, G. & Gupta, A. Variations in the magnetic anisotropy properties of epitaxial CrO_2 films as a function of thickness. *Phys. Rev. B Condens. Matter Mater. Phys.* **71**, 1–7 (2005).
31. Ingvarsson, S., Xiao, G., Parkin, S. S. P. & Gallagher, W. J. Thickness-dependent magnetic properties of $Ni_{81}Fe_{19}$, $Co_{90}Fe_{10}$ and $Ni_{65}Fe_{15}Co_{20}$ thin films. *J. Magn. Magn. Mater.* **251**, 202–206 (2002).
32. Walsh, F. C. Overall rates of electrode reactions. Faraday's laws of electrolysis. *Trans. Inst. Met. Finish.* **69**, 155–157 (1991).
33. Arregi, J. A., Riego, P. & Berger, A. What is the longitudinal magneto-optical Kerr effect?. *J. Phys. D. Appl. Phys.* **50**, aa4ea6 (2017).
34. Barker, D. & Walsh, F. C. Applications of Faraday's laws of electrolysis in metal finishing. *Trans. Inst. Met. Finish.* **69**, 158–162 (1991).
35. Yusrini, M. & Iskandar, I. Y. Influence of grain size on magnetic properties of electroplated NiFe. *Key Eng. Mater.* **328**, 381–384 (2006).
36. Haider, T. A review of magneto-optic effects and its application. *Int. J. Electromagn. Appl.* **7**, 17–24 (2017).
37. Boardman, A. D. & King, N. Magneto-optics and the Kerr effect with ferromagnetic materials. In *Tutorials in Complex Photonic Media* 57–79 (SPIE, 2009). https://doi.org/10.1117/3.832717.Ch3.
38. Ghasemi, R. *et al.* Electrical and magneto-optical characterization of Py/MoS_2 bilayer: A facile growth of magnetic-metal/semi-conductor heterostructure. *Mater. Lett.* **265**, 127454 (2020).
39. Baradaran Ghasemi, A. H., Faridi, E., Ansari, N. & Mohseni, S. M. Extraordinary magneto-optical Kerr effect via MoS_2 monolayer in $Au/Py/MoS_2$ plasmonic cavity. *RSC Adv.* **6**, 106591–106599 (2016).
40. Mosconi, D. *et al.* Site-selective integration of MoS_2 flakes on nanopores by means of electrophoretic deposition. *ACS Omega* **4**, 9294–9300 (2019).
41. Kittel, C. On the theory of ferromagnetic resonance absorption. *Phys. Rev.* **73**, 155–161 (1948).
42. Kalarickal, S. S. *et al.* Ferromagnetic resonance linewidth in metallic thin films: Comparison of measurement methods. *J. Appl. Phys.* **99**, 1–7 (2006).
43. Azzawi, S. *et al.* Evolution of damping in ferromagnetic/nonmagnetic thin film bilayers as a function of nonmagnetic layer thickness. *Phys. Rev. B* **93**, 054402 (2016).
44. Tserkovnyak, Y., Brataas, A. & Bauer, G. E. W. Enhanced Gilbert damping in thin ferromagnetic films. *Phys. Rev. Lett.* **88**, 117601 (2002).
45. Barati, E., Cinal, M., Edwards, D. M. & Umerski, A. Gilbert damping in magnetic layered systems. *Phys. Rev. B* **90**, 014420 (2014).
46. Lenz, K. *et al.* Two-magnon scattering and viscous Gilbert damping in ultrathin ferromagnets. *Phys. Rev. B* **73**, 144424 (2006).
47. Sun, Y. *et al.* Damping in yttrium iron garnet nanoscale films capped by platinum. *Phys. Rev. Lett.* **111**, 106601 (2013).
48. Rojas-Sánchez, J.-C. *et al.* Spin pumping and inverse spin Hall effect in platinum: The essential role of spin-memory loss at metallic interfaces. *Phys. Rev. Lett.* **112**, 106602 (2014).
49. Tserkovnyak, Y., Brataas, A. & Bauer, G. E. W. Spin pumping and magnetization dynamics in metallic multilayers. *Phys. Rev. B* **66**, 224403 (2002).
50. MacNeill, D. *et al.* Control of spin–orbit torques through crystal symmetry in WTe_2/ferromagnet bilayers. *Nat. Phys.* **1**, 300–305 (2016).
51. Shao, Q. *et al.* Strong Rashba–Edelstein effect-induced spin–orbit torques in monolayer transition metal dichalcogenide/ferromagnet bilayers. *Nano Lett.* **16**, 7514–7520 (2016).
52. Zhang, W. *et al.* Research update: Spin transfer torques in permalloy on monolayer MoS_2. *APL Mater.* **4**, 032302 (2016).
53. Cheng, C. *et al. Spin to Charge Conversion in MoS_2 Monolayer with Spin Pumping* 1–15. arXiv:1510.0345 (2015).

Acknowledgements

Author contributions

M.Y.V.: Data curation; Formal analysis; Investigation; Methodology; Writing—original draft. L.J.: Conceptualization; Data curation; Formal analysis; Investigation; Methodology; Supervision; Validation; Writing—original draft; Writing—review & editing. M.Z.: Data curation; Methodology. S.M.M.: Conceptualization; Project administration; Resources; Supervision; Validation; Visualization; Roles/Writing—original draft; Writing—review & editing.

Competing interests

The authors declare no competing interests.

Additional information

Supplementary Information The online version contains supplementary material available at https://doi.org/10.1038/s41598-022-14060-w.

Correspondence and requests for materials should be addressed to S.M.M.

Reprints and permissions information is available at www.nature.com/reprints.

Publisher's note Springer Nature remains neutral with regard to jurisdictional claims in published maps and institutional affiliations.